41st Plasmadynamics and Lasers Conference

Numerical Study of a MHD-Heat Shield

Nicholas J. Bisek[*] and Jonathan Poggie[†]

Air Force Research Laboratory, Wright-Patterson AFB, OH, 45433-7512, USA

and

Iain D. Boyd[‡]

Department of Aerospace Engineering, University of Michigan, Ann Arbor, MI, 48109, USA

Newly developed computational tools are used to compute hypersonic flow around a hemisphere-cylinder which utilizes a magnet located within the body. The magnetic force generated opposes the incoming flow thereby increasing the shock standoff distance and providing heat mitigation to the stagnation region. Several surface temperature scenarios are explored, though none result in significant change to the shock standoff distance. The Hall effect and ion slip phenomena are added to the plasma model through the electrical conductivity tensor and are validated by simulating channel flow between infinitely repeating electrodes with an applied magnetic field. The Hall effect stretches the current in the streamwise direction while ion slip reduces the stretching for the channel flow scenario. In the hemisphere-cylinder scenario, the strong Hall effect significantly lessens the effectiveness of the magnet at increasing the shock standoff distance while Joule heating reduces the effectiveness of heat mitigation observed in the stagnation region.

Nomenclature

B	=	magnetic field magnitude, T
B	=	magnetic field vector
b	=	magnetic field unit vector
C_h	=	nondimensional heat flux, $2q_w/[\rho_\infty u_\infty^3]$
C_p	=	pressure coefficient, $2(p_w - p_\infty)/[\rho_\infty u_\infty^2]$
E	=	electric field magnitude, V/m
E	=	electric field vector
E	=	total energy per volume
e	=	electron charge, 1.6×10^{-19}C
j	=	current density vector
L	=	geometry length, m
N	=	total number density, m^{-3}
n	=	species number density, m^{-3}
p	=	pressure, Pa
q	=	heat flux (translational, rotational, and vibrational)
r	=	radius, m
Re_m	=	magnetic Reynolds number, $\mu_0\,\sigma\,u\,L$
s	=	ion slip coefficient, $(\rho_{\text{neutrals}}/\rho)^2\,\beta_e\,\beta_i$
S_{local}	=	local magnetic-interaction number, $\sigma\,B^2\,r_n/[\rho\,u]$
T	=	temperature, K
u	=	velocity vector (u, v, w), m/s

---

[*]Senior Researcher, Ohio Aerospace Institute, Member AIAA.
[†]Senior Aerospace Engineer, AFRL/RBAC. Associate Fellow AIAA.
[‡]Professor, Associate Fellow AIAA.

u   = velocity magnitude, $\mathrm{m/s}$
α = degree of ionization
β_e = Hall parameter (electrons), $\mu_\mathrm{e}\,\mathrm{B}$
β_i = Hall parameter (ions)
γ = ratio of specific heats
μ_e = electron mobility, $\sigma/e\,n_\mathrm{e}$
μ_0 = permeability of free space, $4\,\pi \times 10^{-7}\ \mathrm{N/A^2}$
ρ = mass density, $\mathrm{kg/m^3}$
σ = electrical conductivity, $\Omega^{-1}\,\mathrm{m}^{-1}$
$\tilde{\sigma}$ = electrical conductivity tensor (including Hall effect and ion slip)
τ = viscous stress
ϕ = electric potential, V
χ = species mole fraction

Subscript

n   = nose
w   = wall
s = species
∞ = free stream

Species

Ar   = argon
Ar^+ = argon ion
e   = electron

I. Introduction

In the late 1950's Kantrowitz[1] and Resler and Sears[2,3] demonstrated the benefits an applied magnetic field has on an incoming weakly ionized flow, a condition typically observed during re-entry. The concept used the magnetic field to produce a magnetic force which opposed the momentum of the freestream flow. Since the majority of the magnetic force is located within the shock layer, the shock standoff distance from the body increased, which reduced the gradients in the layer (including the heat transfer rate).

The potential benefits of this concept generated a lot of research activity as groups refined semi-analytical calculations by making various approximations to the conservation equations. One of the most complete approximate analytic solutions was obtained by Bush, who used a local solution at the stagnation point of the hypersonic flow over an axisymmetric blunt body to predict significant flow declaration in the presence of a magnetic field.[4,5] A decade later, Coakley and Porter computed the first modern Computational Fluid Dynamic (CFD), simulations of the Magnetohydrodynamic (MHD), blunt body problem,[6] but the simulations still required significant simplifications to the governing equations due to limited computing resources available during that period.

To verify Bush's computational predictions, Ziemer carried out experimental measurements of the shock standoff distance for a similar geometry and found reasonable agreement.[7] The first heat transfer measurements for this concept were collected in the experimental work by Wilkinson[8] for Mach 3 ionized argon at the stagnation point of a blunt cone.

While the effects of the magnetic force can be visually observed to increase in the shock standoff distance, the force also increases drag on the vehicle, which can be measured in tunnel experiments with a load cell. In the late 1960's, experimental effort conducted by Kranc *et al.* provided additional experimental validation sets for the continuing computational efforts.[9] In addition to measuring the shock standoff distance, the work measured the increase in drag for two different axisymmetric geometries. These experiments were conducted in a flow regime where both the viscosity and Hall effect are important, and confirmed the increase in the shock standoff distance and total drag on the geometry in the presence of a dipole magnetic field.

Kranc's experiment also exhibited an increase in total heating, which has been attributed to the Hall effect.[10,11] This was unexpected because the thickening of the shock layer reduces gradients within the stagnation region, which should reduce the heat flux to the body. Previous semi-analytic work had predicted that the Hall effect would only reduce the effectiveness of the magnetic force on increasing the shock standoff

distance and total drag.[12] Regardless of this unexpected outcome, it was determined that the large magnetic field strength required to make the technology practical was too heavy to be placed on re-entry vehicles, and, as such, interest and funding of the research area faded.[13]

During the mid to late 1990's a renewed interest in plasma-assisted hypersonics started to generate new research activity.[14–16] This revival of hypersonic-MHD has been credited to many influences including increasing demand for rapid access to space and the numerous advancements in materials necessary for flight-weight MHD technologies. One of the first to reevaluate the technology using modern CFD was Palmer, who performed first-order spatially accurate simulations of the time-dependent Maxwell's equations coupled to the Navier-Stokes equations to analyze a Mars return vehicle.[17] In addition to increasing the shock standoff distance, MHD technology is being applied and investigated to many subsystems required by a hypersonic vehicle, including flow control,[18–23] local heat load mitigation,[24–26] communications blackout,[27] and MHD power extraction.[28–30]

Despite the technical challenges, limited facilities, and financial costs, some recent experimental studies have been performed to explore electromagnetic effects on hypersonic flows.[31–35] While these efforts have provided new insight into electromagnetic phenomena in hypersonic flows and provided additional validation exercises for testing the accuracy of fluid-MHD codes, the rising costs associated with conducting the experiments (i.e., aging facilities and additional safety protocol), greatly limits the number of experiments being conducted. These limitations generate additional demand for high fidelity computational codes that are capable of predicting the complex flows generated by MHD technology.

This paper is a continuation of a computational study of the experimental research conducted by Kranc et al.[9] While the previous results showed an electrical conductivity model based on solutions to Boltzmann's equation provided results consistent with experimental measurements, several additional influences were left unexplored.[36] An axisymmetric version of the MHD code is developed and verified against three-dimensional computations. Several wall boundary conditions, including a fully radiative wall are implemented, but found to have minimal effect on the change in shock standoff distance. A compact tensor notation for accounting for the Hall effect and ion slip through the electrical conductivity tensor is introduced and validated by simulating channel flow between segmented finite electrodes. The Hall effect and ion slip are accounted for in the hemisphere-cylinder simulations which reduce the effectiveness of the magnet and produce Joule heating around the forebody. The local temperature increase reduces the effectiveness of the magnet for heat mitigation.

II.   Method

A.   Governing Equations

Flow-field results are obtained using CFD to solve the Navier-Stokes equations. The CFD computations are executed using The Michigan Aerothermodynamic Navier-Stokes code (LeMANS), which was developed at the University of Michigan.[37,38]

LeMANS is a general 2D/axisymmetric/3D, parallel, unstructured finite-volume CFD code. LeMANS is able to employ a two-temperature or three-temperature model to account for thermal-nonequilibrium and a standard finite rate chemistry model for non-equilibrium chemistry. For a single temperature model (local thermal equilibrium), with MHD but without finite chemistry, the conservation equations are:

$$\frac{\partial \rho_s}{\partial t} + \nabla \cdot (\rho_s \mathbf{u}) = 0 \tag{1}$$

$$\frac{\partial \rho \mathbf{u}}{\partial t} + \nabla \cdot (\rho \mathbf{u}\mathbf{u} + p\mathbf{I} - \tau) = \mathbf{j} \times \mathbf{B} \tag{2}$$

$$\frac{\partial E}{\partial t} + \nabla \cdot ((E + p)\mathbf{u} - \tau \cdot \mathbf{u} + \mathbf{q}) = \mathbf{j} \cdot \mathbf{E} \tag{3}$$

where ρ_s is the density of species s, and $\mathbf{u}$ is the mass averaged bulk velocity vector. LeMANS assumes the fluid is continuous, Newtonian, and uses Stokes' hypothesis when determining the viscous stress τ. The conservation of momentum, Eqn. (2), contains the total density, ρ, the pressure, p, the identity matrix, $\mathbf{I}$, and a 3×3 tensor containing all the products of the components of the velocity vector, as seen in Eqn. (4):

$$\mathbf{uu} = \begin{bmatrix} u^2 & uv & uw \\ vu & v^2 & vw \\ wu & wy & w^2 \end{bmatrix} \tag{4}$$

B.   Magnetohydrodynamics

Magnetohydrodynamic effects ($\mathbf{j}$, $\mathbf{B}$, and $\mathbf{E}$), are determined using a loosely coupled MHD module which is described in detail in Ref. 36. The module operates by solving a generalized form of Ohm's law to determine the electric potential, ϕ, as seen in Eqn. (5):

$$\nabla \cdot \tilde{\sigma} \cdot [-\nabla\phi + \mathbf{u} \times \mathbf{B}] = 0 \tag{5}$$

Noting the magnetic Reynolds number ($Re_m = \mu_0 \, \sigma \, u \, L << 1$) is small for the cases of interest in this work, the induced magnetic field can be assumed negligible.[39] This means only the external applied magnetic field is present in the flow and must be specified. Hall effect and ion slip are included in the simulations by utilizing the electrical conductivity tensor, $\tilde{\sigma}$, as seen in Eqn. (6):

$$\tilde{\sigma} = \frac{\sigma}{(1+s)^2 + \beta_e^2} \left\{ (1+s)\delta_{ij} + \left[s(1+s) + \beta_e^2 \right] \frac{B_i \, B_j}{B^2} - \varepsilon_{ijk}\beta_e \frac{B_k}{B} \right\} \tag{6}$$

where σ is the electrical conductivity of the fluid, B_i represents the components of the magnetic field vector, and B is its magnitude. A derivation of Eqn. (6) is provided in the Appendix. The Hall parameter, β_e, and ion slip coefficient, s, are defined in Eqns. (7) and (8), respectively:

$$\beta_e = \mu_e \, B \tag{7}$$

$$s = \left(\frac{\rho_{\text{neutral}}}{\rho} \right)^2 \beta_e \, \beta_i \tag{8}$$

where μ_e is the mobility of the electrons, ρ_{neutral} is the sum of the neutral species, and $\beta_i = \mu_i \, B$. The electron mobility is determined directly from the electrical conductivity ($\mu_e = \sigma/e\,n_e$). The ion mobility is determined by setting the ratio of mobilities to a constant. Using values reported in literature,[40,41] the ratio of mobilities is set to 400 ($\mu_e/\mu_i = 400$), unless otherwise specified.

Investigation of the electrical conductivity tensor reveals the ion slip coefficient is only appreciable when its magnitude is on the order of one or larger. Since the ratio of mobilities is constant ($\mu_e/\mu_i = 400$), the Hall parameter must be on the order of 10 or greater before the ion slip coefficient becomes substantial.
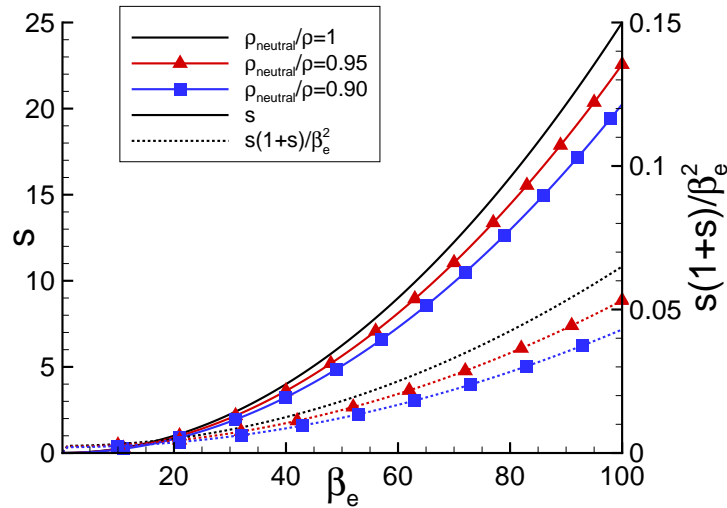

Figure 1.   Hall parameter versus ion slip coefficient for various ionization fractions.

Figure 1 plots the ratio of $s(1+s)$ over β_e^2. This curve indicates when the ion slip coefficient may become important since the terms in the ratio appear in the second term of Eqn. (6). As seen in the figure, $s(1+s)/\beta_e^2$ remains relatively small even though the ion slip coefficient is on the order of ten. Thus, the influence ion slip has on the electrical conductivity tensor remains minor while $\beta_e \leq 100$.

C. The Hall Effect and Ion Slip

Validation of the Hall effect and ion slip was performed by utilizing a computational study developed by Hurwitz *et al.*,[42] and rigorously explored by Oliver and Mitchner.[43] In the numerical experiment, finite segmented electrodes were infinitely repeated along the two walls of a channel, as seen in Fig. 2. An externally applied magnetic field was employed perpendicular to the channel velocity, **u**.
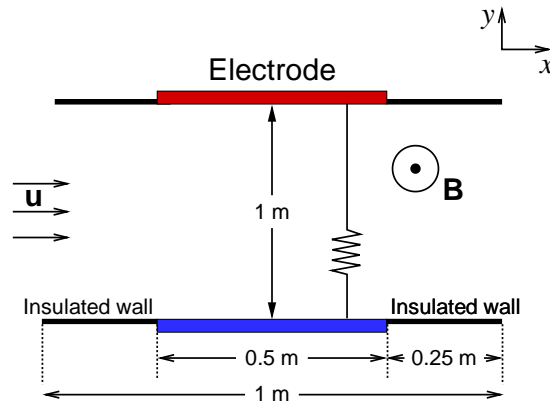

Figure 2. Schematic of the channel flow with finitely segmented electrodes.

Because the channel was infinitely long, periodic boundary conditions were developed and employed at the domain inlet and outlet. Oliver and Mitchner demonstrated that two of the four 'global' conditions (i.e., streamwise and spanwise current or voltage), were required to determine a unique solution.[43] In this validation exercise, the applied voltage between the electrode pairs and neighbors were specified (streamwise and spanwise voltages).

A two-point overlapping stencil, shown in Fig. 3, transfers information between the periodic inlet and outlet, while either adding or subtracting the specified streamwise voltage, $\Delta\phi_x$. Since solutions for the interior cells are computed using a non-uniform, second order stencil, the two point stencil provides sufficient information to accurately update the adjacent interior points. Using this approach, a row of cells starts at the inlet and ends at the outlet (constant y). The inlet ghost cell is set equal to the last interior cell next to the outlet (minus the applied streamwise voltage). Likewise, the outlet's ghost cell is set equal to the interior cell adjacent to the inlet (plus the applied streamwise voltage).
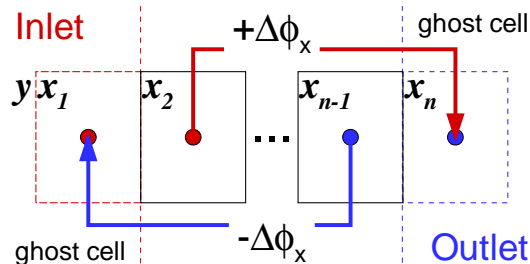

Figure 3. Cartoon of a two point stencil used for period boundary conditions.

Oliver and Mitchner formulated this problem so that the fluid velocity field did not affect the solution as long as $\nabla \times (\mathbf{u} \times \mathbf{B}) = 0$. During one iteration of the flow solver, the MHD routine is executed assuming the velocity profile is only a function of the distance between the plates $\mathbf{u} = f(y)$, which satisfies $\nabla \times (\mathbf{u} \times \mathbf{B}) = 0$

as long as $\mathbf{B} = f(z)$. The velocity profile was assumed to be fully developed Poiseuille flow between parallel plates,[44] as seen in Eqn. (9):

$$\mathbf{u} = f(y) = u_{\text{max}}(1 - \frac{(y - y_h)^2}{h^2})$$

(9)

where u_{max} is the maximum velocity and was set to unity for this scenario ($u_{\text{max}} = 1$ m/s). The y location was measured from the center of the channel width ($y_h = 0.5$ m), so $h = 0.5$ m was the channel half-width.

A grid was developed based on the grid convergence study preformed previously for similar three-dimensional simulations.[36] The grid utilized exponential spacing along the wall surface such that cell clustering occurs near the junction between the insulated wall and the electrode. Exponential spacing was employed between the two walls such that cell clustering occurs near each surface. The grid employed 100 points along the wall ($x-$direction) and 60 points between the walls.

For the scenario with Hall effect, a one tesla uniform magnetic field was externally applied perpendicular to both the streamwise flow and the spanwise voltage. The applied spanwise voltage between an electrode pair was set to one volt, but the spanwise electrode pair was offset by 0.28 m for the Hall parameter of one ($\beta_e = 1$), as seen in Fig. 4. Hurwitz et al. also specified the applied streamwise voltage ($\Delta\phi_x = 0.4305$ V).[42]
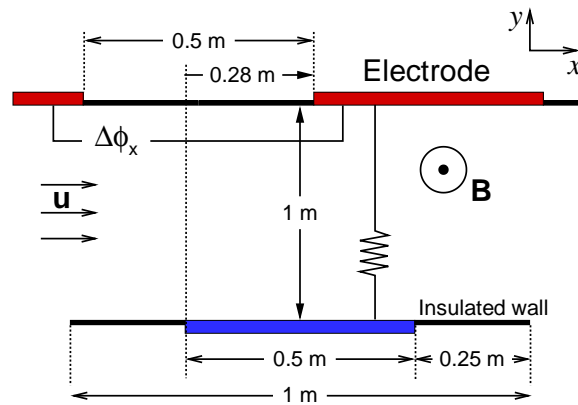

Figure 4. Schematic of channel flow with finitely segmented electrodes used by Hurwitz et al. with Hall effect ($\beta_e = 1$).

The inclusion of the Hall effect allows the magnetic effects into the antisymmetric components of the electrical conductivity tensor, as seen in Eqn. (6). These components 'stretch' the streamwise component of the current density vector, j_x. Hurwitz et al. computed the potential and electric field, as seen in Fig. 5. Current flows along a diagonal of the squares shown in Fig. 5(a) (i.e., the current lines cross the orthogonal squares in the figures).[40]
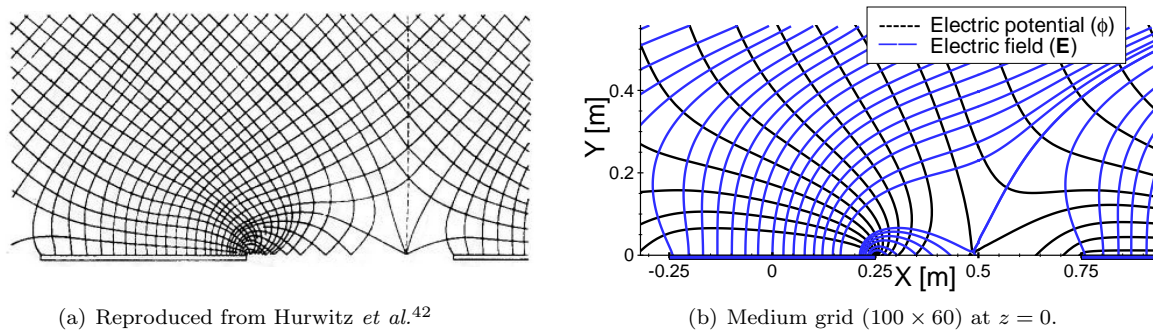

(a) Reproduced from Hurwitz et al.[42]

(b) Medium grid (100×60) at $z = 0$.

Figure 5. Potential contours and electric field streamlines between segmented electrodes with the Hall effect. ($\mathbf{B}_z = 1$ T, $\sigma = 1\,\Omega^{-1}\text{m}^{-1}$, $\beta_e = 1$, and $\Delta\phi_x = 0.4305$ V)

While the computed solution closely resembles Hurwtiz's semi-analytic solution, it is not identical. Hurwitz assumed a negligible streamwise current ($j_x = 0$), when the solution was sufficiently away from the wall

(i.e., $y = 0.5$ m). While this approximation allowed an analytical solution to be determined, it is not completely accurate, and is not enforced in the computations performed here. Nonetheless, the figures portray similar characteristics, and indicate that the Hall effect was successfully implemented.

The ion slip parameter acts to reduce the stretching of the streamwise current. Figure 6 plots the current lines for Hurwtiz's scenario with and without ion slip. The ion slip coefficient was set to one (s = 1) for the simulation. While this scenario is unphysical unless the flow's ion mobility is greater than its electron mobility (i.e., $\rho_{neutral}/\rho \leq 1$ therefore $\beta_i > 1$ since $\beta_e = 1$), it does illustrate the influence of the ion slip coefficient.
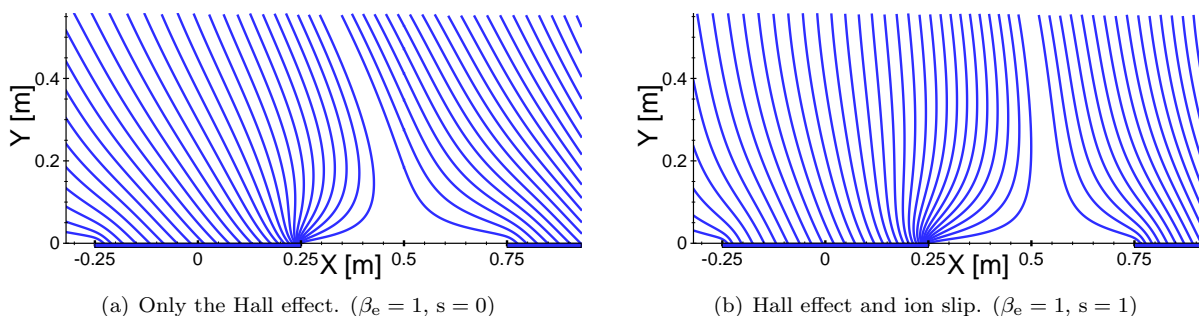

(a) Only the Hall effect. ($\beta_e = 1$, s = 0)

(b) Hall effect and ion slip. ($\beta_e = 1$, s = 1)

Figure 6. Current streamlines between segmented electrodes with the Hall effect and ion slip. ($B_z = 1$ T, $\sigma = 1\,\Omega^{-1}\mathrm{m}^{-1}$, and $\Delta\phi_x = 0.4305$ V)

Since ion slip allows the ions to carry more of the current, the current lines appear more vertical in the center of the channel ($y = 0.5$ m), which is qualitatively consistent with results obtained by Gaitonde for a similar scenario.[45] Likewise, the angle at which the current enters electrodes is also reduced, which should reduce the spanwise impedance between the electrode pair.

D. Electrical Conductivity

The experiment performed by Kranc *et al.* used pre-ionized argon (Ar, Ar$^+$, and e). The electrical conductivity profile for weakly-ionized argon is shown in Fig. 7. As seen in the figure, the electrical conductivity exhibits two distinct regions, namely, weakly ionized (T $\lesssim$ 10,000 K) and fully ionized (T > 10,000 K). Both regions display exponential growth versus temperature, which means a highly accurate model is critical to accurately predict the electrical conductivity across the entire temperature range.
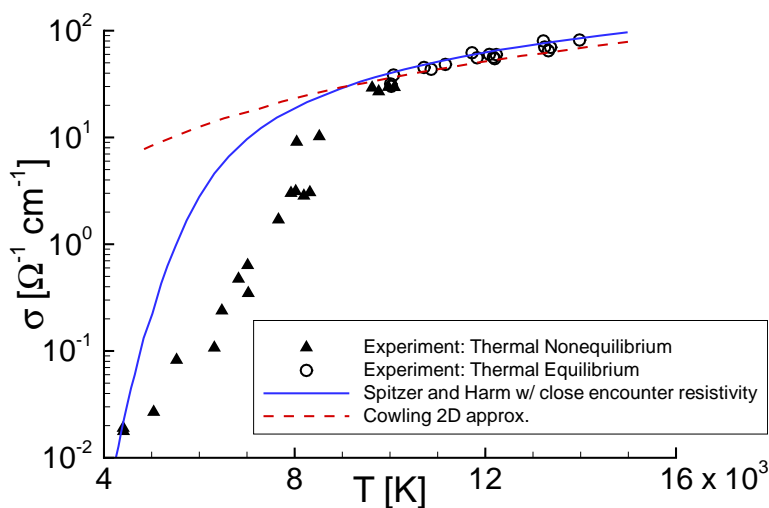

Figure 7. Electrical conductivity of argon ($p = 0.013$ atm), reproduced from Lin *et al.*[46]

Previous work explored different electrical conductivity models for the MHD-Heat Shield study and found

the conductivity model based on a polynomial response surface (PRS) to solutions of Boltzmann's equation provided solutions to the change in shock standoff distance that agreed reasonably well with experimental measurements.[36] The 2nd PRS model is shown in Eqn. (10):

$$\sigma = \frac{\chi_e}{\exp\left(\mathbf{PRS}\right)}$$

$$
\begin{aligned}
\mathbf{PRS} = & -842.64 + 128.02(\mathrm{E}/N) + 2558.28(\chi_{\mathrm{Ar}}) - 4112.52(\chi_{\mathrm{Ar}^+}) \\
& - 4.82(\mathrm{E}/N)^2 - 118.25(\mathrm{E}/N)(\chi_{\mathrm{Ar}}) - 121.33(\mathrm{E}/N)(\chi_{\mathrm{Ar}^+}) \\
& - 1732.34(\chi_{\mathrm{Ar}})^2 + 3229.51(\chi_{\mathrm{Ar}})(\chi_{\mathrm{Ar}^+}) - 7342.51(\chi_{\mathrm{Ar}^+})^2
\end{aligned}
\tag{10}
$$

where E/N is the normalized electric field, and χ_s is the species mole fractions. This definition of the model requires the normalized electric field to be re-normalized from 0 to 1 for a range of 0.01 to 100 Td. (1 townsend [Td] $= 10^{-17}$ V·cm^2) The species mole fractions (χ_s), are used directly in the equation. This model was developed for an ionized mole fraction less than one percent (i.e., $\chi_{\mathrm{Ar}^+} < 0.01$). However, the model could be expanded to accommodate a larger range of mole fractions if necessary.

E.   Viscosity Model

Chemically non-reacting, thermodynamic equilibrium simulations were computed using the variable hard sphere (VHS) viscosity model. The VHS model was used because the viscosity is assumed to only be a function of temperature, since the species present (argon, argon ion, and electrons), have a single energy mode and were chemically non-reacting:

$$\mu = \mu_{\mathrm{ref}} \left(\frac{T}{T_{\mathrm{ref}}} \right)^{\omega} \tag{11}$$

where μ is the viscosity, the reference viscosity coefficient, $\mu_{\mathrm{ref}} = 2.117 \times 10^{-5}$ N s/m^2, for a reference temperature, $T_{\mathrm{ref}} = 273$ K, and a viscosity index, $\omega = 0.81$. This method, as outlined by Schwartzentruber et al.,[47] requires several reference coefficients which are listed in Ref. 48.

III.   Hemisphere-Cylinder Results

Three-dimensional calculations were carried out for Mach 4.75 argon flow over a hemisphere-cylinder, which was originally studied experimentally by Kranc et al.[9] The forebody hemisphere has a radius of 0.75 inch ($r_n = 0.01905$ m), and the geometry was mounted parallel to the freestream, as seen in Fig. 8.
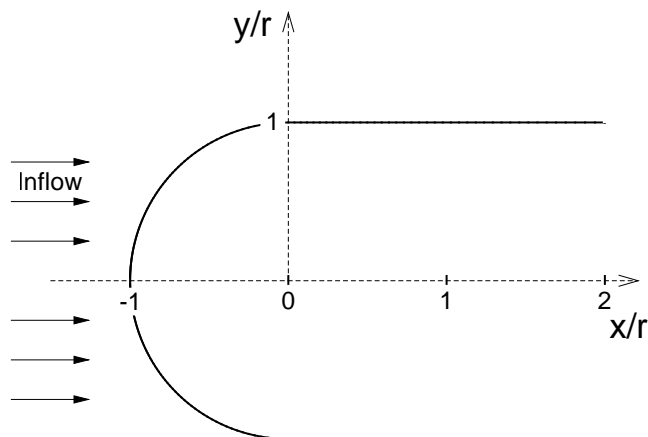

Figure 8.   Hemisphere capped geometry. Adapted from Ref. 9.

The freestream flow was composed of strongly ionized argon (the degree of ionization was estimated by Kranc *et al.* as $\alpha = 0.025$), which was produced by a plasma torch (direct-current arc-heater). The heater was located before the converging-diverging nozzle, which accelerates the gas into the test chamber. Kranc *et al.* state that the electrons were 'frozen' in the nozzle, and that the flow was not chemically reacting after it was partially ionized by the heater. Previous work showed Kranc *et al.* may have overestimated the freestream ionization fraction,[36] which was updated using the Saha equation for a singly ionized atomic gas.[49] The 'adjusted' flow conditions used in this analysis and are listed in Table 1.

Table 1. Flow conditions for the MHD-Heat Shield experiment in argon.

Parameter	Value	
M	4.75	
u_∞	3000.0	m/s
T_∞	1100.0	K
T_w	300.0	K
p_∞	27.8	Pa
ρ_∞	1.1×10^{-4}	kg/m³
n_e	1.03×10^{19}	m⁻³
α	0.00623	
r_n	0.01905	m
μ_∞	8×10^{-5}	kg/m·s

A.   Magnetic Field

In the experiment of Kranc *et al.*, the applied magnetic field was produced by an electromagnet located inside the hemisphere-shaped forebody. The electromagnetic was approximately 1 inch (0.0254 m), long by 1.25 inch (0.03175 m), in diameter with a 0.375 inch (0.0095 m) core. The core was composed of vanadium permandur and the windings were made of #19 Anaconda HML (Polyimide Enamel) coated wire with a magnetic resistance of 0.5 Ω.[9] Measurements made by Kranc *et al.* found the magnet behaved like an ideal dipole near the stagnation region of the flow, and was modeled as such for this analysis.

The magnetic field decays as r^{-3} from its centroid, which was assumed to be located along the x-axis, where the forebody merges with the rest of geometry ($x/r_\mathrm{n} = 0$), as seen in Fig. 9. The magnetic moment was aligned along the x-axis and was positioned to oppose the incoming flow along the stagnation line. The magnetic field contours in the figure are nondimensionalized by the peak magnetic field strength, B_max, which occurs at the stagnation point ($x/r_\mathrm{n} = -1$). Note that the peak magnetic field strength is used to designate each simulation for the rest of this analysis.

In Cartesian coordinates, the ideal dipole magnetic field is:

$$\mathbf{B} = \frac{-B_\mathrm{max}}{2\left(x^2 + y^2 + z^2\right)^{5/2}} \begin{bmatrix} 2x^2 - (y^2 + z^2) \\ 3xy \\ 3xz \end{bmatrix} \tag{12}$$

The negative sign in front of the peak field strength, B_max, is due to the direction of the field flux. The centroid of the dipole is located at the origin of the coordinate system, though the computational domain does not contain the magnetic field centroid.

B.   Grid Convergence

A structured grid was generated using two grid domains. The first domain includes the hemispherical forebody, while the second accommodates the rest of the geometry. A grid convergence study was conducted for the baseline flow in previous work.[36] While this is sufficient for simulations without MHD effects, a more complete convergence study also verifies the grid is sufficiently resolved in the presence of the magnetic field. The magnetic field in the presence of a pre-ionized gas presents an additional challenge because it is initially
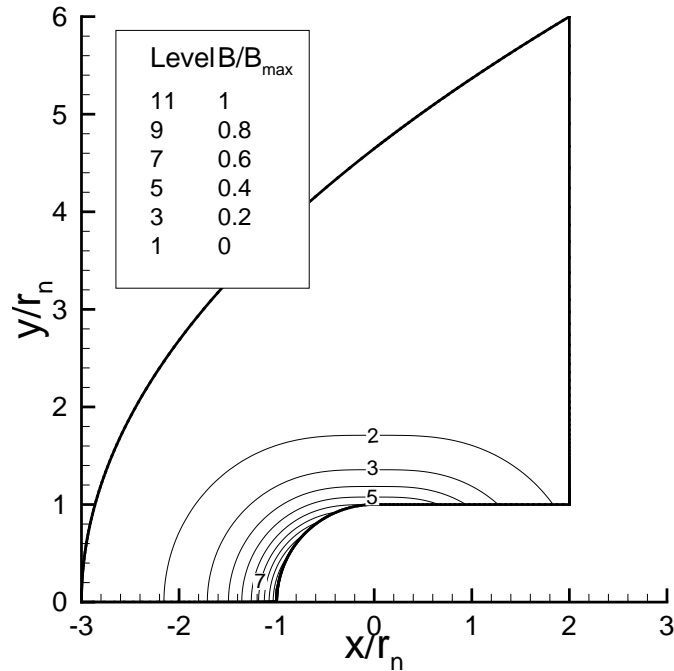
Figure 9. Nondimensional dipole magnetic field contours from a magnet located in the hemisphere capped geometry.

unclear how much the flow field will change because of the magnetic field (i.e., how large does the domain need to be to capture the magnetic effects on the flow).

The grid was generated with equal spacing along the hemisphere portion of the geometry (first domain), and gradually increases in spacing along the remaining surface (second domain). Grid points were equally spaced around the circumference of the geometry and the radial points were algebraically spaced to increase the number of points close to the body. As a result, cell clustering occurred primarily in the hemispherical forebody and near the body surface. The 'coarse' grid uses 50 points along the body (30 points in the hemispherical region), 30 points along one quarter of the circumference, and 30 radial points. Two doubly refined grids were also developed and used in the grid convergence study, giving the following set of computational meshes: $50 \times 30 \times 30$ (coarse), to $100 \times 60 \times 60$ (medium), to $200 \times 120 \times 120$ (fine).

Since the flow experiences an increase in shock standoff distance due to the presence of a magnetic field, it is also important to ensure grid independence when the magnetic fields are present. To this end, simulations were also computed in the presence of a large magnetic field ($B_{max} = 0.45$ T). These simulations neglected the Hall effect. However, the Hall effect should diminish the effectiveness of the magnetic field at influencing the shock location. Therefore, the grid study solutions neglecting Hall effect provide sufficient resolution even when the Hall effect and ion slip are present.

Figure 10 plots the pressure coefficient and nondimensional heat flux for both the baseline flow and the flow with the magnetic field along the surface of the geometry, as defined in Eqns. (13) and (14), respectively:

$$C_p = \frac{p_w - p_\infty}{1/2 \, \rho_\infty u_\infty^2} \tag{13}$$

$$C_h = \frac{q_w}{1/2 \, \rho_\infty u_\infty^3} \tag{14}$$

where q_w is the total heat flux to the wall.

The grid convergence study showed little difference between the 'medium' and 'fine grids for both the baseline scenario and the scenario with an applied magnetic field $B_{max} = 0.45$ T. Therefore, the 'medium' grid spacing was considered sufficiently refined.

The magnetic-interaction number is the ratio of the magnetic body force to the inertia force. This global nondimensional number helps predict when flows will be influenced by the presence of a magnetic field, but
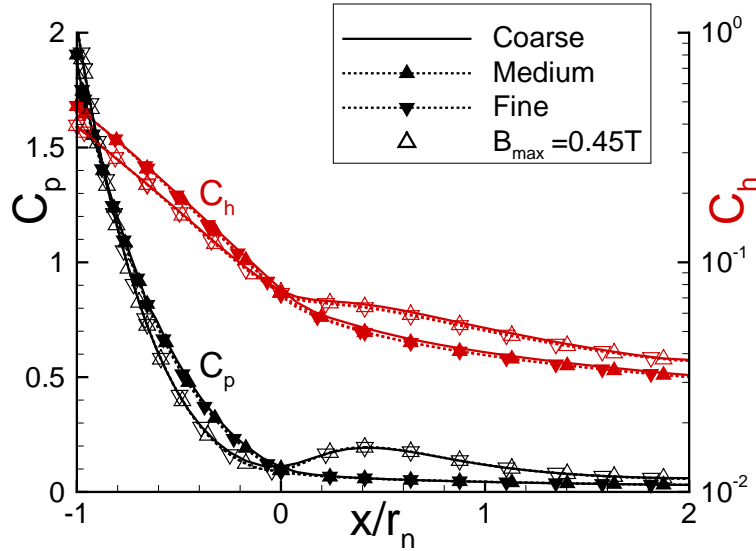
Figure 10. Nondimensional pressure and heat flux along the surface of Mach 4.75 argon flow around a hemisphere-cylinder for various grids.

is traditionally applied to flows that are not pre-ionized.[40]

Because the freestream flow was sufficiently pre-ionized, the freestream electrical conductivity allowed the applied magnetic field to influence the flow-field upstream of the shock. In order to estimate the proper domain size required to account for the expected changes in the flow-field due to the presence of an applied magnetic field, a local magnetic-interaction number was developed, as seen in Eqn. (15).

$$S_{local} = \frac{\sigma\,B^2\,r_n}{\rho\,u} \tag{15}$$

where u is the magnitude of the local velocity.

The baseline flow-field solution is used to estimate the electrical conductivity and a large magnetic field ($B_{max} = 0.45$ T), was applied to the domain. With these values, the local magnetic-interaction was estimated, as seen in Fig. 11.

As seen in the figure, the magnetic interaction number decreases as the magnetic field strength decays. Using these contours as a guide, two additional grids were created. The first extends radially along the x-axis to $x/r_n = -3$, while the second only extends to $x/r_n = -2.5$. These sizes correspond to $S_{local} \geq 0.01$ and $S_{local} \geq 0.05$, respectively. Figure 12 plots the temperature contours with an applied magnetic field of $B_{max} = 0.45$ T for these grids.

As seen in Fig. 12, the computed flow-field is unable to fully extend from the body as the domain size is reduced. From the figures it appears that a reasonable solution is obtained if the domain is large enough to ensure $S_{local} \geq 0.01$ along the stagnation line (x-axis). To verify this, the baseline solution was used to estimate the local magnetic-interaction for a magnetic field of $B_{max} = 0.6$ T, as seen in Fig. 13.

Maintaining $S_{local} \geq 0.01$ along the stagnation line, a grid was developed to extend to $x/r_n = -3.5$. Figure 14 shows the flow-field is not significantly influenced by the domain reduction. Since the maximum magnetic field strength employed in the analysis is $B_{max} = 0.45$ T, the grid extending to $x/r_n = -3$ was employed for the rest of the analysis.

This paper estimates the leading edge of the shock to correspond to the location where the density ratio exceeds the ideal gas infinite Mach number threshold for a normal shock wave along the stagnation line:

$$\lim_{M_1 \to \infty} \frac{\rho_2}{\rho_1} = \frac{\gamma + 1}{\gamma - 1} \tag{16}$$

where γ is the ratio of specific heats, ρ_1 is the freestream density, and ρ_2 is the downstream density. Using this equation, the density ratio limit for argon is four ($\gamma = 5/3$).

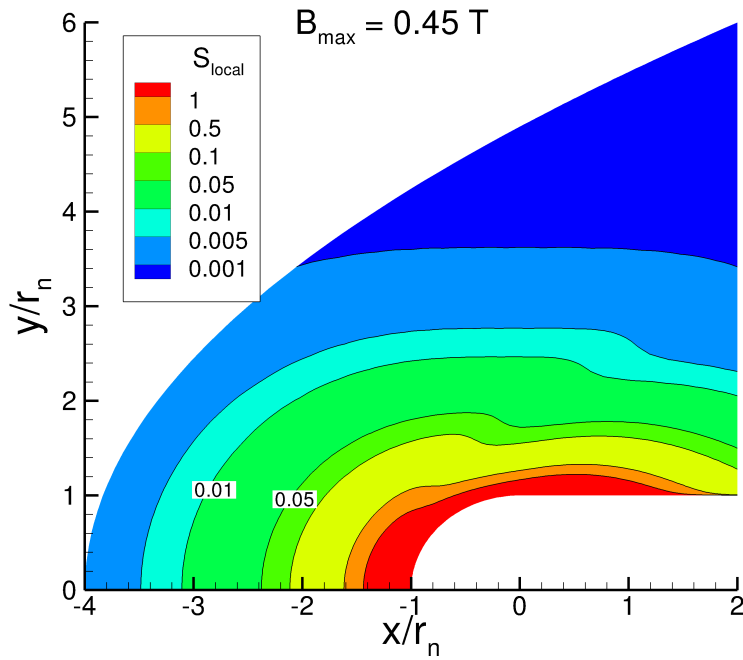American Institute of Aeronautics and Astronautics Paper 2010-4487

Figure 11. Contours of the local magnetic-interaction number for Mach 4.75 argon flow around a hemisphere-cylinder using the baseline flow-field solution. ($B_{max} = 0.45$ T)

(a) Grid extent based on $S_{local} \geq 0.01$ contour.
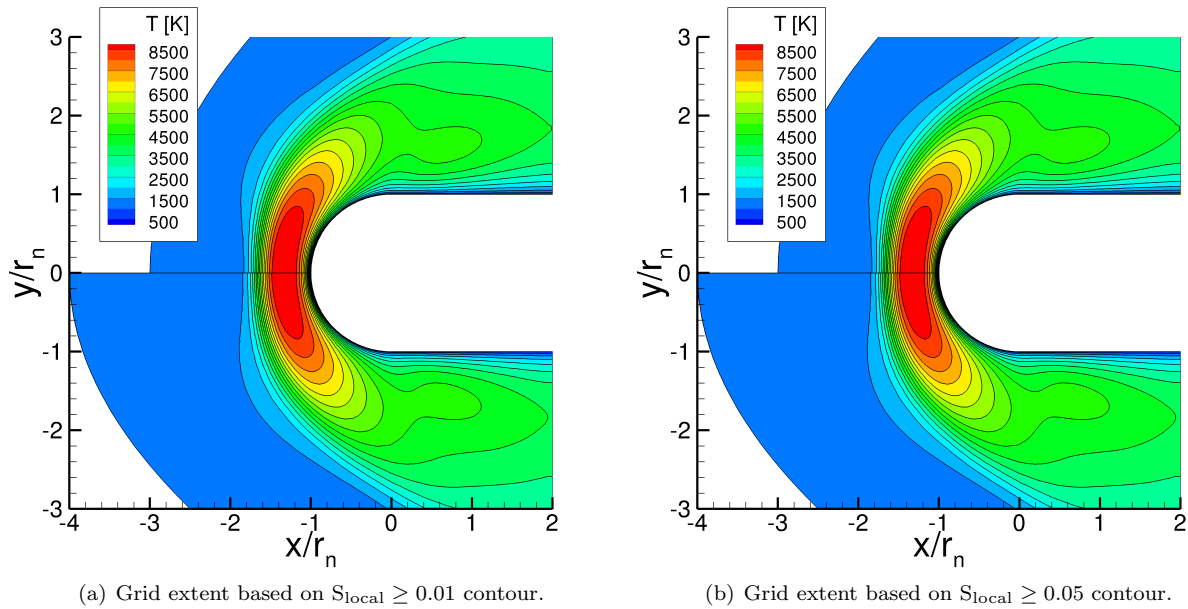
(b) Grid extent based on $S_{local} \geq 0.05$ contour.

Figure 12. Temperature contours for Mach 4.75 argon flow around a hemisphere-cylinder with various domain sizes. ($B_{max} = 0.45$ T) Bottom: extended grid.

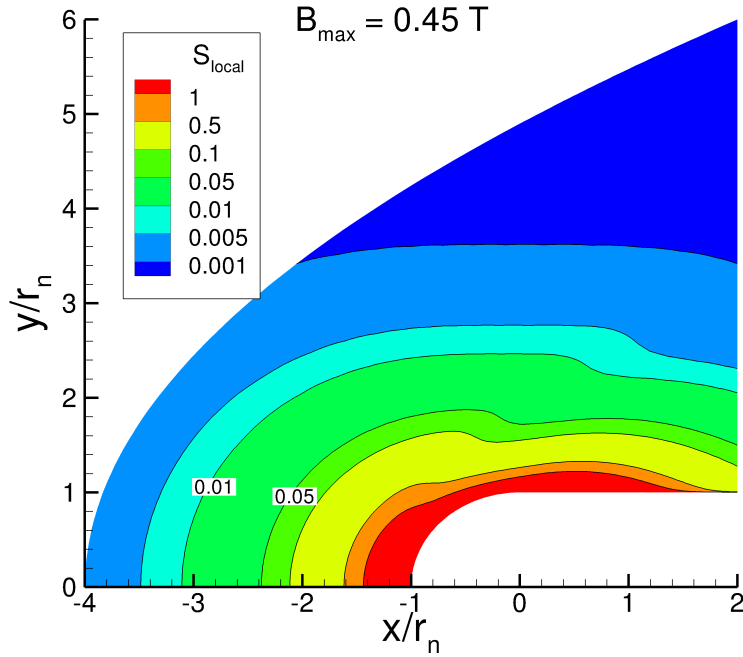American Institute of Aeronautics and Astronautics Paper 2010-4487

Figure 13. Local magnetic-interaction number contours for Mach 4.75 argon flow around a hemisphere-cylinder using the baseline flow-field solution. ($B_{max} = 0.60$ T)

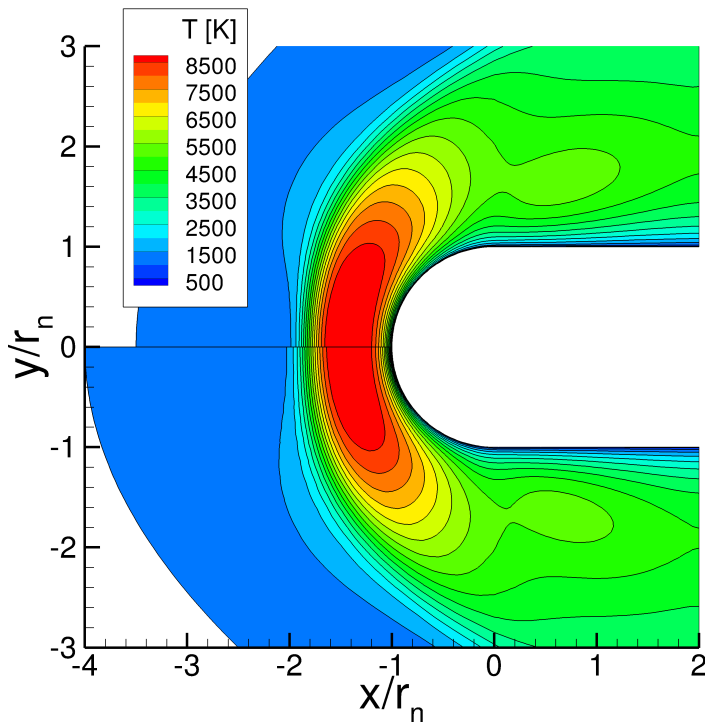**Figure 14. Temperature contours for Mach 4.75 argon flow around a hemisphere-cylinder with various domain sizes. ($B_{max} = 0.60$ T) Bottom: extended grid.**

C. Hot Wall Effects

Previous work assumed the hemisphere-cylinder held a constant wall temperature of 300 K. This assumption was made because the actual surface temperature was unknown, the magnet was being actively cooled by a water bath, and because the experiment's short run times would have limited the surface heating. To verify this assumption, a set of simulations was computed assuming the surface has a constant wall temperature of 1000 K. In addition, another set of simulations was computed assuming the wall temperature was in radiative equilibrium using the Stefan-Boltzmann Law ($T_{\mathrm{w}}^4 = \mathrm{q_w}/\epsilon\,\sigma^*$).

Three peak magnetic field strengths were explored for the different wall conditions. Figure 15 plots the density ratio on the stagnation line for a peak magnetic field strength of 0.45 T. The fully radiative wall temperature varied from 950 K along the cylinder portion of the geometry to 1800 K at the stagnation point.
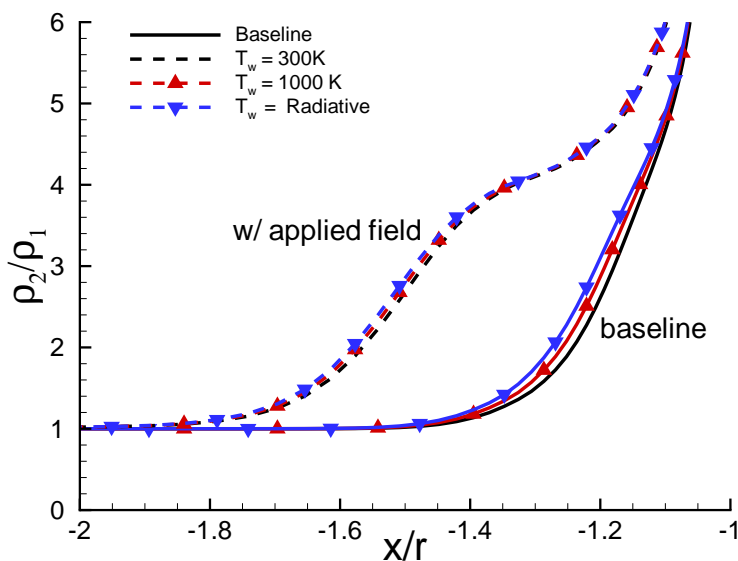

Figure 15. Density ratio on the stagnation line for Mach 4.75 argon flow around a hemisphere-cylinder with a dipole magnetic field for various wall temperature boundary conditions. ($\mathbf{B_{max}} = 0.45$ T, $\beta_{\mathbf{e}} = 0$)

While the various wall conditions do influence the actual location of the shock, the change in shock standoff distance was not significantly influenced, as seen in Table 2. Therefore a constant wall temperature of 300 K was assumed sufficient and used in the rest of the analysis.

Table 2. Percent change in shock standoff distance for various magnetic field strengths and wall conditions. ($\beta_{\mathbf{e}} = 0$)

$\mathbf{B_{max}}$	$T_{\mathbf{w}} = 300$ K	$T_{\mathbf{w}} = 1000$ K	$T_{\mathbf{w}} = $ Radiative Equilibrium
0.13	2.5%	1.2%	2.3%
0.28	10.6%	9.2%	9.7%
0.45	23.5%	22.5%	21.6%

D. Hall Effect and Ion Slip

The flow-field around the geometry (without the applied magnetic field), is axisymmetric and steady, as evident in the temperature contours seen in Fig. 16. Without the Hall effect the electric field can be shown to be zero[4] and, thus, the electric current must only travel in the azimuthal direction (perpendicular to the incoming flow, around the axis of symmetry). This reduces the magnetic force in the momentum equation to $\tilde{\sigma} \cdot (\mathbf{u} \times \mathbf{B}) \times \mathbf{B}$, and sets the energy deposition term in the total energy equation to zero, $\mathbf{j} \cdot \mathbf{E} = 0$. Note that Joule heating is still present under these assumptions, $(\mathbf{E} + \mathbf{u} \times \mathbf{B}) \cdot \mathbf{j} \neq 0$.
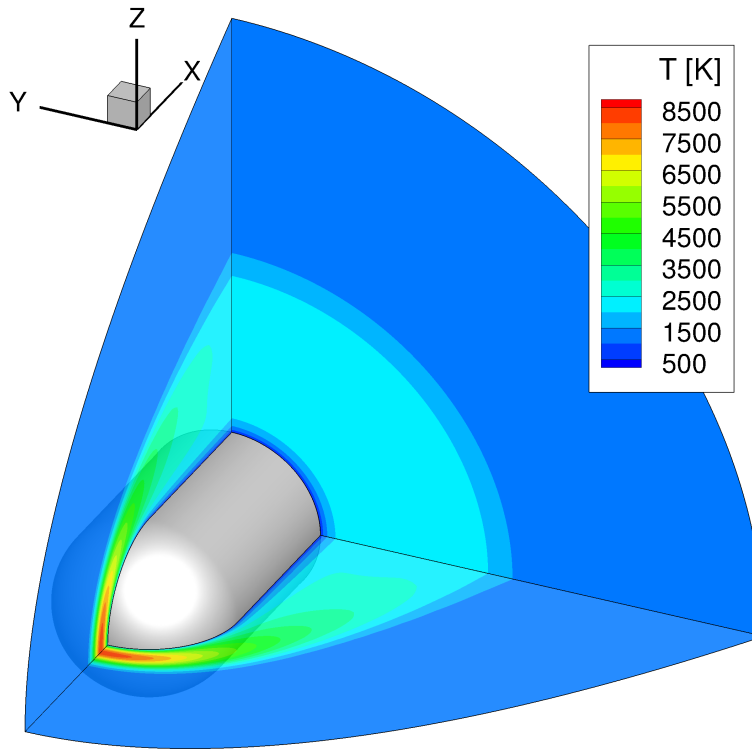
Figure 16. Temperature contours for Mach 4.75 argon flow around a hemisphere-cylinder.

Although the baseline flow-field is axisymmetric, the Hall effect and ion slip create antisymmetric terms in the conductivity tensor. This means it is no longer justifiable to assume the electric field is zero. In addition, the current is now primarily located in the meridian planes (i.e., planes that contain the x-axis), with a weakened current still present in the azimuthal direction. These effects result in a torque on the magnet, or since computations are computed in a relative frame (i.e., the geometry and magnet are fixed and the fluid is moving), the current lines corkscrew toward the geometry, as seen in Fig. 17.

The current lines twist to the right (i.e., clockwise), while they are located over the hemisphere portion of the geometry due to the direction of the magnetic moment. However, the current lines switch rotation direction (i.e, counter-clockwise), along the cylinder portion of the geometry because the change in direction of the magnetic field lines changes the direction of the force acting on the electrons.

Figure 18 shows the Hall parameter contours for the flow with an applied magnetic field of 0.13 T. Because the flow is pre-ionized, the Hall parameter is quite large for the flow, especially near the stagnation region. The strong Hall effect almost completely diminishes the increase in shock standoff distance observed in previous work without the Hall effect,[36] a result that is consistent with findings by Porter *et al.*,[12] though the study is still ongoing.

In addition to weakening the effectiveness of the magnetic force at increasing shock standoff distance, the presence of the electric field results in an increase in total heating to the fluid domain ($\mathbf{j} \cdot \mathbf{E} \neq 0$). The increase in total temperature slightly increases the heat flux to the geometry surface (versus the same scenario without accounting for the Hall effect).

IV.   Conclusions

Recently developed computational tools were used to compute hypersonic flow around a hemisphere capped geometry which utilizes a magnet located within the body as a means of heat flux mitigation. These tools include a procedure to accurately account for the Hall effect and ion slip. These phenomena produce antisymmetric components of the electrical conductivity tensor which lead to a stretching of the current streamlines in the direction of the flow.

Mach 4.75 argon flow over a hemisphere-cylinder corresponding to the experiment conducted by Kranc
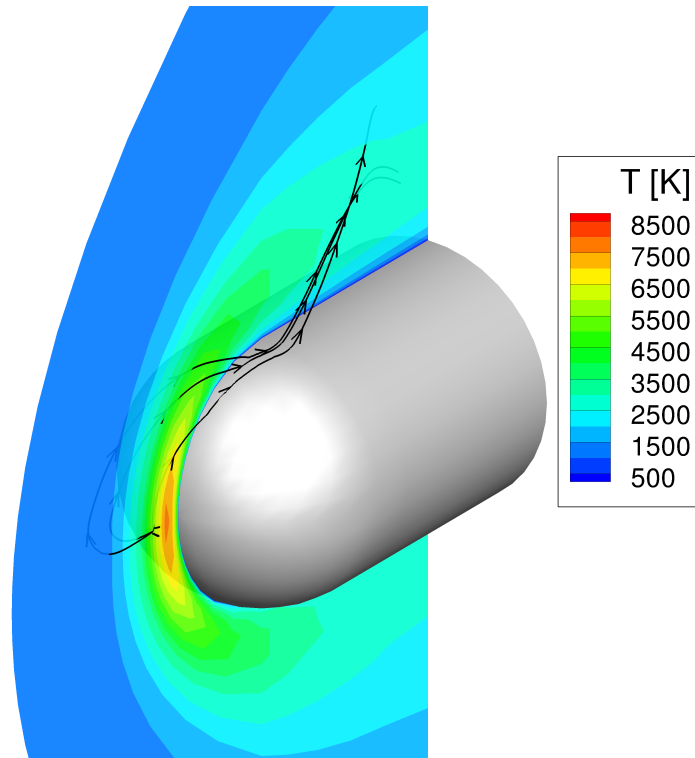
Figure 17. Temperature contours and current lines for Mach 4.75 argon flow around a hemisphere-cylinder with a 0.13 T magnetic field (including Hall effect and ion slip).
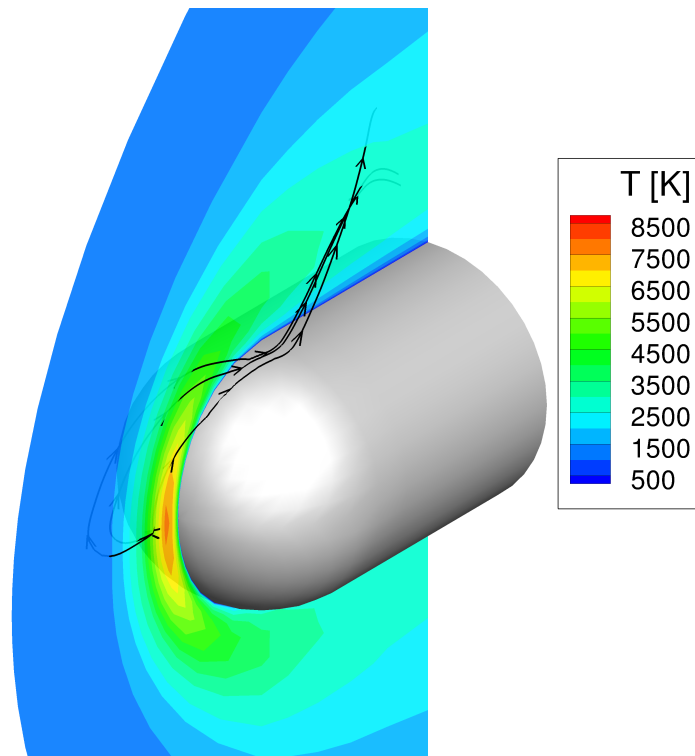

Figure 18. Hall coefficient contours for Mach 4.75 argon flow around a hemisphere-cylinder with a 0.13 T magnetic field.

et al. was investigated computationally using modern CFD techniques. Because the geometry surface temperature was unknown in the experiment, several approaches were computationally explored, but the change in shock standoff distance did not greatly depend on the surface temperature. Simulations were also computed with the Hall effect and ion slip. Compared to simulations without these phenomena, the Hall effect and ion slip reduced the effectiveness of the magnetic force at increasing the shock standoff distance while producing additional heating in the flow through Joule heating. Since the Hall parameter is directly related to the magnitude of the magnetic field, use of weaker magnetic fields should reduce the negative implications of these phenomena. However, weaker fields are less effective at increasing the shock standoff distance and thereby providing sufficient heat mitigation.

These results have important implications for design of MHD-Heat Shield devices: they can reduce peak heat loads, but with a potential penalty in total heating. Since both peak and total heat load are important aspects to consider when designing a thermal protection system, this technology provides additional scenarios for vehicle designers to evaluate.

References

[1]Kantrowitz, A. R., "A Survey of Physical Phenomena Occurring in Flight at Extreme Speeds," *Proceedings of the Conference on High-Speed Aeronautics*, edited by A. Ferri, N. J. Hoff, and P. A. Libby (Polytechnic Institute of Brooklyn, New York, 1955), pp. 335 − 339.

[2]Resler, E. L. and Sears, W. R., "The Prospects for Magneto-Aerodynamics," *Journal of Aeronatuical Sciences*, Vol. 25, April 1958, pp. 235–245, 258.

[3]Resler, E. L. and Sears, W. R., "The Prospects for Magneto-Aerodynamics Correction and Addition," *Journal of Aero/Space Sciences*, Vol. 26, No. 5, May 1959, pp. 318.

[4]Bush, W. B., "Magnetohydrodynamic-Hypersonic Flow Past a Blunt Body," *Journal of Aerospace Sciences*, Vol. 25, 1958, pp. 685.

[5]Bush, W. B., "The Stagnation-Point Boundary Layer in the Presence of an Applied Magnetic Field," *Journal of Aerospace Sciences*, Vol. 28, No. 8, August 1961, pp. 610–611, 630.

[6]Coakley, J. F. and Porter, R. W., "Time-Dependent Numerical Analysis of MHD Blunt Body Problem," *AIAA Journal*, Vol. 9, No. 8, August 1971, pp. 1624–1626.

[7]Ziemer, R. W., "Experimental Investigations in Magnetoaerodynamics," *Journal of American Rocket Society*, Vol. 29, No. 9, 1959, pp. 642.

[8]Wilkinson, B., "Magnetohydrodynamic Effects on Stagnation-Point Heat Transfer from Partially Ionized Nonequilibrium Gases in Supersonic Flow," *Engineering Aspects of Magnetohydrodynamics: Proceedings, 3rd Symposium*, edited by N. W. Mather and G. W. Sutton (Gordon and Breach, New York, 1964), pp. 413 − 438.

[9]Kranc, S., Yuen, M. C., and Cambel, A. B., "Experimental Investigation of Magnetoaerodynamic Flow around Blunt Bodies," Tech. rep., National Aeronautics and Space Administration, Washington, D.C., August 1969, NASA CR-1392.

[10]Nowak, R. J., Kran, S., Porter, R. W., Yuen, M. C., and Cambel, A. B., "Magnetogasdynamic Re-Entry Phenomena," *Journal of Spacecraft*, Vol. 4, No. 11, November 1967, pp. 1538–1542.

[11]Nowak, R. J. and Yuen, M. C., "Heat Transfer to a Hemispherical Body in Supersonic Argon Plasma," *AIAA Journal*, Vol. 11, No. 11, November 1973, pp. 1463–1464.

[12]Porter, R. W. and Cambel, A. B., "Hall Effect if Flight Magnetogasdynamics," *AIAA Journal*, Vol. 5, No. 12, December 1967, pp. 2208–2213.

[13]Romig, M. F., "The Influence of Electric and Magnetic Fields on Heat Transfer to Electrically Conducting Fluids," *Advances in Heat Transfer*, edited by T. F. Irvine and J. P. Hartnett (Academic, New York, 1964), Vol. 1, pp. 267 − 354.

[14]Fomin, V. M., Tretyakov, P. K., and Taran, J.-P., "Flow Control using Various Plasma and Aerodynamic Approaches," *Aerospace Science and Technology*, Vol. 8, No. 5, July 2004, pp. 411–421.

[15]Shang, J. S., Surzhikov, S. T., Kimmel, R., Gaitonde, D., Menart, J., and Hayes, J., "Mechanisms of Plasma Actuators for Hypersonic Flow Control," *Progress in Aerospace Sciences*, Vol. 41, No. 8, November 2005, pp. 642–668.

[16]Bityurin, V., Bocharov, A., and Lineberry, J., "MHD Flow Control in Hypersonic Flight," *13th International Space Planes and Hypersonic Systems Technologies Conference*, AIAA Paper 2005-3225.

[17]Palmer, G., "Magnetic Field Effects on the Computed Flow over a Mars Return Aerobrake," *Journal of Thermophysics and Heat Transfer*, Vol. 7, No. 2, April-June 1993, pp. 294–301.

[18]Girgis, I. G., Shneider, M. N., Macheret, S. O., Brown, G. L., and Miles, R. B., "Creation of Steering Moments in Supersonic Flow by Off-Axis Plasma Heat Addition," *40th AIAA Aerospace Sciences Meeting and Exhibit*, AIAA Paper 2002-129.

[19]Kremeyer, K., Sebastian, K., and Shu, C.-W., "Computational Study of Shock Mitigation and Drag Reduction by Pulsed Energy Lines," *AIAA Journal*, Vol. 44, No. 8, August 2006, pp. 1720–1731.

[20]Menart, J., Stanfield, S., Shang, J., Kimmel, R., and Hayes, J., "Study of Plasma Electrode Arrangements for Optimum Lift in a Mach 5 Flow," *44th AIAA Aerospace Sciences Meeting and Exhibit*, AIAA Paper 2006-1172.

[21]Yan, H. and Gaitonde, D., "Control of Edney IV Interaction by Energy Pulse," *44th AIAA Aerospace Sciences Meeting and Exhibit*, AIAA Paper 2006-562.

[22]Gnemmi, P., Charon, R., Dupéroux, J.-P., and George, A., "Feasibility Study for Steering a Supersonic Projectile by a Plasma Actuator," *AIAA Journal*, Vol. 46, No. 6, June 2008, pp. 1308–1317.

[23]Bisek, N. J., Boyd, I. D., and Poggie, J., "Numerical Study of Plasma-Assisted Aerodynamic Control for Hypersonic Vehicles," *Journal of Spacecraft and Rockets*, Vol. 46, No. 3, May-June 2009, pp. 568–576.

[24]Bityurin, V. A., Vatazhin, A. B., and Gus'kov, O. V., "Hypersonic Flow Past the Spherical Nose of a Body in the Presence of a Magnetic Field," *Fluid Dynamics*, Vol. 39, No. 4, July 2004, pp. 657–666.

[25]Miles, R. B., Macheret, S. O., Shneider, M. N., Steeves, C., Murray, R. C., Smith, T., and Zaidi, S. H., "Plasma-Enhanced Hypersonic Performance Enabled by MHD Power Extraction," *43rd AIAA Aerospace Sciences Meeting and Exhibit*, AIAA Paper 2005-561.

[26]Katsurayama, H., Kawamura, M., Matsuda, A., and T., A., "Kinetic and Continuum Simulations of Electromagnetic Control of a Simulated Reentry Flow," *Journal of Spacecraft and Rockets*, Vol. 45, No. 2, March-April 2008, pp. 248–254.

[27]Kim, M., Keidar, M., and Boyd, I. D., "Analysis of an Electromagnetic Mitigation Scheme for Reentry Telemetry Through Plasma," *Journal of Spacecraft and Rockets*, Vol. 45, No. 6, November-December 2008, pp. 1223–1229.

[28]Macheret, S. O., Shneider, M. N., and Candler, G. V., "Modeling of MHD Power Generation on Board Reentry Vehicles," *42nd AIAA Aerospace Sciences Meeting*, AIAA Paper 2004-1024.

[29]Wan, T., Suzuki, R., Candler, G., Macheret, S., and Schneider, M., "Three Dimensional Simulation of Electric Field and MHD Power Generation During Re-Entry," *36th AIAA Plasmadynamics and Lasers Conference*, AIAA Paper 2005-5045.

[30]Fujino, T., Yoshino, T., and Ishikawa, M., "Prediction of Generator Performance and Aerodynamic Heating of Reentry Vehicle Equipped with On-board Surface Hall Type MHD Generator," *39th Plasmadynamics and Lasers Conference*, AIAA Paper 2008-4225.

[31]Bityurin, V., Bocharov, A., and Lineberry, J., "Results of Experiments on MHD Hypersonic Flow Control," *35th AIAA Plasmadynamics and Lasers Conference*, AIAA Paper 2004-2263.

[32]Takizawa, Y., Sato, S., Abe, T., and Konigorski, D., "Electro-Magnetic Effect on Shock Layer Structure in Reentry-Related High-Enthalpy Flow," *35th AIAA Plasmadynamics and Lasers Conference*, AIAA Paper2004-2162.

[33]Kimmel, R., Hayes, J., Menart, J., and Shang, J., "Supersonic Plasma Flow Control Experiments," Tech. rep., U.S. Air Force Research Laboratory, Wright-Patterson AFB, OH, December 2005, ARFL-VA-WP-TR-2006-3006.

[34]Matsuda, A., Kawamura, M., Takizawa, Y., Otsu, H., Konigorski, D., Sato, S., and Abe, T., "Experimental Investigation of the Hall Effect for the Interaction between the Weakly-Ionized Plasma Flow and Magnetic Body," *45th AIAA Aerospace Sciences Meeting*, AIAA Paper 2007-1437.

[35]Gülhan, A., Esser, B., Koch, U., Siebe, F., Riehmer, J., Giordano, D., and Konigorski, D., "Experimental Verification of Heat-Flux Mitigation by Electromagnetic Fields in Partially-Ionized-Argon Flows," *Journal of Spacecraft and Rockets*, Vol. 46, No. 2, March-April 2009, pp. 274–283.

[36]Bisek, N. J., Boyd, I. D., and Poggie, J., "Numerical Study of Magnetoaerodynamic Flow around a Hemisphere," *Journal of Spacecraft and Rockets*, (accepted for publication).

[37]Scalabrin, L. C. and Boyd, I. D., "Development of an Unstructured Navier-Stokes Solver For Hypersonic Nonequilibrium Aerothermodynamics," *38th AIAA Thermophysics Conference*, AIAA Paper 2005-5203.

[38]Scalabrin, L. C. and Boyd, I. D., "Numerical Simulation of Weakly Ionized Hypersonic Flow for Reentry Configurations," *9th AIAA/ASME Joint Thermophysics and Heat Transfer Conference*, AIAA Paper 2006-3773.

[39]Shercliff, J., "A Textbook of Magnetohydrodynamics," Pergamon Press, 1965.

[40]Sutton, G. W. and Sherman, A., "Engineering Magnetohydrodynamics," McGraw-Hill, 1965.

[41]Raizer, Y. P., "Gas Discharge Physics," Springer-Verlag, 1991.

[42]Hurwitz Jr., H., Kilb, R. W., and Sutton, G. W., "Influence of Tensor Conductivity on Current Distribution in MHD Generator," *Journal of Applied Physics*, Vol. 32, No. 2, February 1961, pp. 205–216.

[43]Oliver, D. A. and Mitchner, M., "Nonuniform Electrical Conduction in MHD Channel," *AIAA Journal*, Vol. 5, No. 8, August 1967, pp. 1424–1432.

[44]White, F. M., "Viscous Fluid Flow, 3rd ed." McGraw-Hill, 2006.

[45]Gaitonde, D. V., "A High-Order Implicit Procedure for the 3-D Electric Field in Complex Magnetogasdynamic Simulations," *Computers and Fluids*, Vol. 33, No. 3, March 2004, pp. 345–374.

[46]Lin, S.-C., Resler, E. L., and Kantrowitz, A., "Electrical Conductivity of Highly Ionized Argon Produced by Shock Waves," *Journal of Applied Physics*, Vol. 26, No. 1, January 1955, pp. 95–109.

[47]Schwartzentruber, T. E., Scalabrin, L. C., and Boyd, I. D., "Hybrid Particle-Coontinuum Simulations of Non-Equilibrium Hypersonic Blunt Body Flow Fields," *9th AIAA/ASME Joint Thermophysics and Heat Transfer Conference*, AIAA Paper 2006-3602.

[48]Bird, G. A., "Molecular Gas Dynamics and the Direct Simulation of Gas Flows," Oxford University Press, 1994.

[49]Messerle, H. K., "Magnetohydrodynamic Electrical Power Generation," John Wiley & Sons, Inc., 1995.

[50]Mitchner, M. and Kruger Jr., C. H., "Partially Ionized Gases," John Wiley and Sons, Inc., 1973.

Appendix

Equation 6 is formulated by starting from the definition of the generalized form of Ohm's Law, including Hall effect and ion slip, but neglecting the electron pressure gradient:[50]

$$\mathbf{j} = \sigma \left[\mathbf{E} + \mathbf{u} \times \mathbf{B} \right] - \beta_e \cdot \mathbf{j} \times \mathbf{b} - s \cdot \mathbf{b} \times (\mathbf{j} \times \mathbf{b}) \tag{17}$$

where β_e and s are the Hall parameter and ion slip coefficient, which are defined in Eqns. (7) and (8), respectively. It is important to note that $\mathbf{B}$ is the magnetic field vector, while $\mathbf{b} = \mathbf{B}/B$ is the magnetic field unit vector.

Setting $\mathbf{E}' = \mathbf{E} + \mathbf{u} \times \mathbf{B}$, and combining terms, Eqn. (17) is written as:

$$\sigma\mathbf{E}' = \begin{pmatrix} 1 + \frac{s}{B^2}\left(B_y^2 + B_z^2\right) & \frac{\beta_e}{B}B_z - \frac{s}{B^2}B_xB_y & -\frac{\beta_e}{B}B_y - \frac{s}{B^2}B_xB_z \\ -\frac{\beta_e}{B}B_z - \frac{s}{B^2}B_xB_y & 1 + \frac{s}{B^2}\left(B_x^2 + B_z^2\right) & \frac{\beta_e}{B}B_x - \frac{s}{B^2}B_yB_z \\ \frac{\beta_e}{B}B_y - \frac{s}{B^2}B_xB_z & -\frac{\beta_e}{B}B_x - \frac{s}{B^2}B_yB_z & 1 + \frac{s}{B^2}\left(B_x^2 + B_y^2\right) \end{pmatrix}\mathbf{j} \tag{18}$$

Setting the matrix in Eqn. (18) to be equal to $\mathbf{M} = (M_0, M_1, M_2)$, where M_i is a column vector, allows Ohm's law to be reformulated for the current density by determining the inverse of $\mathbf{M}$ (i.e., $\mathbf{j} = \sigma\mathbf{M}^{-1} \cdot \mathbf{E}'$):

$$\mathbf{M}^{-1} = \frac{1}{det(\mathbf{M})}\begin{pmatrix} (M_1 \times M_2)^T \\ (M_2 \times M_0)^T \\ (M_0 \times M_1)^T \end{pmatrix} = \frac{1}{det(\mathbf{M})}\begin{pmatrix} c_{11} & c_{12} & c_{13} \\ c_{21} & c_{22} & c_{23} \\ c_{31} & c_{32} & c_{33} \end{pmatrix} \tag{19}$$

$$
\begin{aligned}
det(\mathbf{M}) &= (1+s)^2 + \beta_e^2 \\[1em]
c_{11} &= 1 + s + \left[s(1+s) + \beta_e^2\right]\frac{B_x^2}{B^2} \\[1em]
c_{12} &= \left[s(1+s) + \beta_e^2\right]\frac{B_xB_y}{B^2} - \beta_e\frac{B_z}{B} \\[1em]
c_{13} &= \left[s(1+s) + \beta_e^2\right]\frac{B_xB_z}{B^2} + \beta_e\frac{B_y}{B} \\[1em]
c_{21} &= \left[s(1+s) + \beta_e^2\right]\frac{B_yB_x}{B^2} + \beta_e\frac{B_z}{B} \\[1em]
c_{22} &= 1 + s + \left[s(1+s) + \beta_e^2\right]\frac{B_y^2}{B^2} \\[1em]
c_{23} &= \left[s(1+s) + \beta_e^2\right]\frac{B_yB_z}{B^2} - \beta_e\frac{B_x}{B} \\[1em]
c_{31} &= \left[s(1+s) + \beta_e^2\right]\frac{B_zB_x}{B^2} - \beta_e\frac{B_y}{B} \\[1em]
c_{23} &= \left[s(1+s) + \beta_e^2\right]\frac{B_zB_y}{B^2} + \beta_e\frac{B_x}{B} \\[1em]
c_{33} &= 1 + s + \left[s(1+s) + \beta_e^2\right]\frac{B_z^2}{B^2}
\end{aligned}
\tag{20}
$$

Noting the repeated terms, the matrix can be written compactly in tensor notation using the Kronecker delta (δ_{ij}), and the Levi-Civita symbol (ε_{ijk}):

$$c_{ij} = (1+s)\delta_{ij} + \left[s(1+s) + \beta_e^2\right]\frac{B_i B_j}{B^2} - \varepsilon_{ijk}\beta_e\frac{B_k}{B} \tag{21}$$

Equation (21) is combined with previous solutions to yield a compact form for the electrical conductivity tensor, which is the same as Eqn. (6):

$$\tilde{\sigma} = \frac{\sigma}{(1+s)^2 + \beta_e^2}\left\{(1+s)\delta_{ij} + \left[s(1+s) + \beta_e^2\right]\frac{B_i B_j}{B^2} - \varepsilon_{ijk}\beta_e\frac{B_k}{B}\right\} \tag{22}$$

Note that the dimensional formulation described in Eqn. (6) can be recovered from Gaitonde's non-dimensional formulation[45] by replacing $R_H\,\beta$ with $\beta_e/[\sigma\,B]$ and $I_s\,\alpha$ with $s/[\sigma\,B^2]$.